A Wideband Oscillator Exploiting Multiple Resonances in Lithium Niobate MEMS Resonator

Ali Kourani, *Graduate Student Member, IEEE*, Ruochen Lu, *Member, IEEE*, and Songbin Gong, *Senior Member, IEEE*

***Abstract*— This article presents a comprehensive guide to codesign lithium niobate ($LiNbO_3$) lateral overtone bulk acoustic resonators (LOBARs) and voltage-controlled oscillators (VCOs) using discrete components on a printed circuit board (PCB). The analysis focuses on understanding the oscillator-level tradeoffs between the number of locked tones, frequency stability, tuning range, power consumption, and phase noise. Moreover, this article focuses on understanding the relationship between the abovementioned specifications and the different LOBAR parameters, such as electromechanical coupling (k_t^2), quality factor (Q), transducer design, and the resonator size. As a result of this study, the first voltage-controlled MEMS oscillator (VCMO) based on $LiNbO_3$ LOBAR is demonstrated. Our LOBAR excites over 30 resonant modes in the range of 100–800 MHz with a frequency spacing of 20 MHz. The VCMO consists of an LOBAR in a closed loop with two amplification stages and a varactor-embedded tunable *LC* tank. By adjusting the bias voltage applied to the varactor, the tank can be tuned to change the closed-loop gain and phase responses of the oscillator so that the Barkhausen conditions are satisfied for a particular resonant mode. The tank is designed to allow the proposed VCMO to lock to any of the ten overtones ranging from 300 to 500 MHz. These ten tones are characterized by average Qs of 2100, k_t^2 of 1.5%, figure of merit (FOM = Qk_t^2) of 31.5 enabling low phase noise, and low-power oscillators crucial for Internet of Things (IoT). Due to the high Qs of the $LiNbO_3$ LOBAR, the measured VCMO shows a close-in phase noise of −100 dBc/Hz at 1-kHz offset from a 300-MHz carrier and a noise floor of −153 dBc/Hz while consuming 9 mW. With further optimization, this VCMO can lead to direct radio frequency (RF) synthesis for ultralow-power transceivers in multimode IoT nodes.**

***Index Terms*— Lithium niobate, MEMS, oscillator, overtone, phase noise, synthesizers.**

I. Introduction

RADIO frequency (RF) synthesizers are the heartbeat of any wireless transceiver and Internet-of-Things (IoT) transceivers are no exception. Generating frequency-stable wideband RF carriers consumes a significant portion of the power budget for battery-powered devices [1]. Therefore, miniature, low-power, low phase noise, and wide tuning range RF synthesizers are becoming highly desirable for battery-powered multiband and multistandard IoT transceivers.

To synthesize spectrally pure RF signals, either indirect synthesis based on the phase-locked loops (PLLs) locked to a quartz crystal (XTAL) [2], [3] or directly constructing signals digitally for the follow-on digital-to-analog conversion (DAC) [4], [5] can be adopted. PLLs based on XTALs are the state of the art (SOA) for producing RF carriers with superior close-in phase noise. However, their large footprint, low frequency of operation, and limited frequency tunability hinder their adaptation for IoT [6], [7]. On the other hand, direct digital synthesizers provide fast settling time, fine frequency resolution, and small area. Yet, their high noise floor, large power consumption, and spurious nature are challenging for any battery-powered IoT transceiver.

As an alternative approach to both XTALs and digital methods, direct RF synthesis based on piezoelectric acoustic/MEMS is emerging for multimode IoT systems due to its potential to deliver low power, low phase noise, and wide tuning range. Fundamentally, its promised high performance arises from high Q [8]–[10], large electromechanical coupling (k_t^2) [11], and high figure of merit (FOM = Qk_t^2). The high Q ensures a good phase noise performance, whereas the large k_t^2 permits wide tuning range voltage-controlled MEMS oscillators (VCMOs). In combination, k_t^2 and Q (i.e., FOM) are crucial for low power consumption. Among various MEMS resonator options, laterally vibrating resonators (LVRs) have been garnering most interest for providing the abovementioned characteristics when high-performance piezoelectric materials are adopted (i.e., doped aluminum nitride (AlN) [12]–[14] or lithium niobate ($LiNbO_3$) [15]–[24]).

Unfortunately, LVRs to date are typically designed to produce a single resonance, thus limiting the oscillator tuning range to about 1.4% [24]. Although switching between many LVRs within an oscillator can extend the range [25]–[28], such an approach is prone to fabrication yield issues and higher costs. On the other hand, using a single resonator with multiresonances can help to reduce parallelism without sacrificing performance. For this reason, dual-mode MEMS resonators [29], [30], and more recently lateral overtone bulk

Manuscript received January 24, 2020; accepted April 13, 2020. Date of publication April 22, 2020; date of current version August 27, 2020. *(Corresponding author: Ali Kourani.)*

The authors are with the Electrical and Computer Engineering Department, University of Illinois at Urbana–Champaign, Urbana, IL 61801 USA (e-mail: kourani2@illinois.edu).

Digital Object Identifier 10.1109/TUFFC.2020.2989623

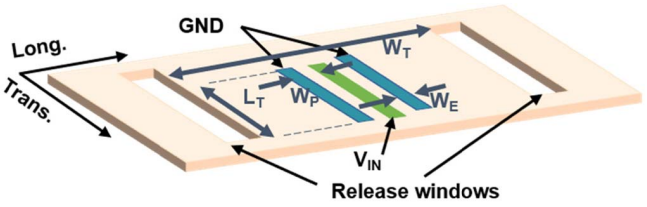

Fig. 1. Schematic of an LOBAR.

acoustic resonators (LOBAR) leveraging the equally spaced harmonics in $LiNbO_3$ thin-film cavity, have been explored. In contrast to its predecessors, namely, high-overtone bulk acoustic resonators (HBARs) [31]–[35] and LOBARs based on AlN [36]–[38], $LiNbO_3$ LOBARs [39]–[41] showed much higher FOMs for multiple equally spaced resonances surpassing the SOA.

Hence, overmoding a $LiNbO_3$ LVR can give rise to a more advanced direct RF synthesis.

This article presents the first $LiNbO_3$ LOBAR-based VCMO exploiting multiple overtones in a single resonator. This VCMO features low phase noise, low power consumption, wide tuning range, and small form factor suited for multimode IoT nodes. The demonstrated VCMO is capable of locking to ten overtones that are excited in a single LOBAR with a noncontiguous tunable oscillation frequency ranging from 300 to 500 MHz. It also shows a measured close-in phase noise of −100 dBc/Hz at 1-kHz offset from a 300-MHz carrier and a noise floor of −153 dBc/Hz while consuming 9 mW.

The rest of this article is organized as follows. Section II discusses the design of a $LiNbO_3$ LOBAR in the context of using it later to implement a wideband VCMO enabling direct RF synthesis for multimode IoT applications. Section III then focuses on the design and simulated performance of our VCMO. Different design tradeoffs between the number of locked tones, frequency stability, tuning range, power consumption, and phase noise will be discussed. Moreover, the study will focus on understanding the relationship between the oscillator specifications and different LOBAR parameters, such as k_t^2, Q, transducer design, and the resonator size. Section IV reports on the oscillator measurement results. Finally, Section V concludes this article.

II. Lithium Niobate LOBARs

A. Overview

As shown in Fig. 1, the LOBAR consists of aluminum interdigitated electrodes (IDEs) partially covering the top surface of a suspended $LiNbO_3$ thin film. The resonator width (W_T) is significantly larger than the electrodes (W_E) and the gap widths (W_G) needed for the overmode operation. The orientation of the device is chosen as $-10°$ to the $+y$-axis in the x-cut plane of $LiNbO_3$ for exciting a family of shear horizontal (SH) modes of various lateral mode orders characterized by high k_t^2 [42]. Key dimensional parameters of a typical LOBAR using two transducers (three IDEs) are shown in Fig. 1.

In contrast to a conventional resonator targeting the excitation of a single resonant mode, LOBARs excite several equally

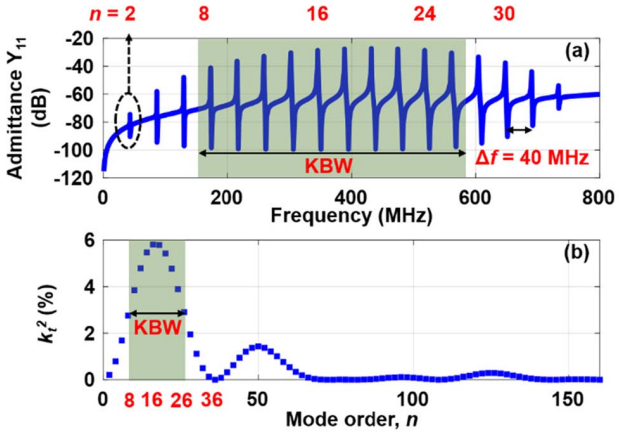

Fig. 2. Simulated response of a two transducer LOBAR using the model demonstrated in [40]. (a) Admittance response. (b) k_t^2. Parameters used in the simulation: $W_T = 100$ μm, $W_E = W_G = 2.5$ μm, $C_o = 180$ fF, and $Q = 2000$ for all tones.

spaced resonances simultaneously. These modes are principally the eigenmodes of the resonant cavity. Assuming a small ratio of the film thickness (h) to the acoustic wavelength (λ) for the frequency range of interest, the frequencies of different resonant modes (f_n) can be approximated by

$$f_n = \frac{n v_{SH0}}{2W_T} \tag{1}$$

where f_n is the resonant frequency of the nth-order mode and v_{SH0} is the SH0 mode phase velocity.

Based on the simplified model demonstrated in [40], the LOBAR characteristics are shown in Fig. 2. For resonances further away from the center frequency (f_{center}), the modes are less excited, hence a reduced k_t^2. This is because the transducer cannot uniformly couple energy to all the modes. It couples energy most efficiently to a mode (n) that corresponds to the center frequency (f_{center}) of the resonator. f_{center} is set by the transducer pitch (W_P) as

$$f_{center} = \frac{v_{SH0}}{2W_P}. \tag{2}$$

The resonant mode is most effectively excited when $W_P = \lambda/2$. The coupling decreases when W_P and λ mismatch and becomes 0 when $W_P = \lambda$ due to the full cancellation of mutual energy. The third specification is the electromechanical coupling bandwidth (KBW) of the resonator, defined as the frequency range where various modes are excited with not less than half of k_t^2 at f_{center}. The fourth specification of the LOBAR is the frequency spacing (Δf) between the adjacent tones, which can be expressed as

$$\Delta f = \frac{v_{SH0}}{W_T}. \tag{3}$$

Apart from the frequency-related specifications mentioned earlier, the device static capacitance C_o, Q, and k_t^2 of each tone are the most important specifications for building oscillators. C_o is mostly set by the IDE dimensions, the thickness of the resonator, and the materials used. This static capacitance identifies the minimum power consumption of the VCMO as will be seen in this article. Q, affecting the phase noise of the

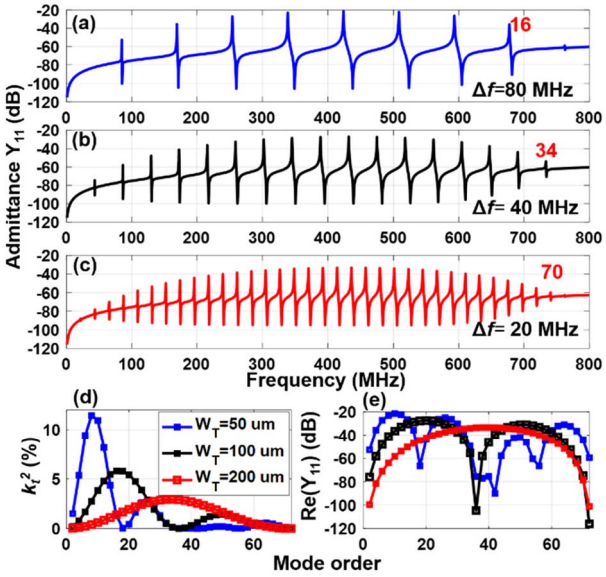

Fig. 3. Admittance of the LOBAR with (a) $W_T = 50$ μm, (b) $W_T = 100$ μm, and (c) $W_T = 200$ μm. (d) k_t^2 and (e) $1/R_m$ of LOBAR with $W_T = 50$, 100, and 200 μm. $W_E = W_G = 2.5$ μm, $C_o = 180$ fF, and $Q = 2000$ values are used in these simulations.

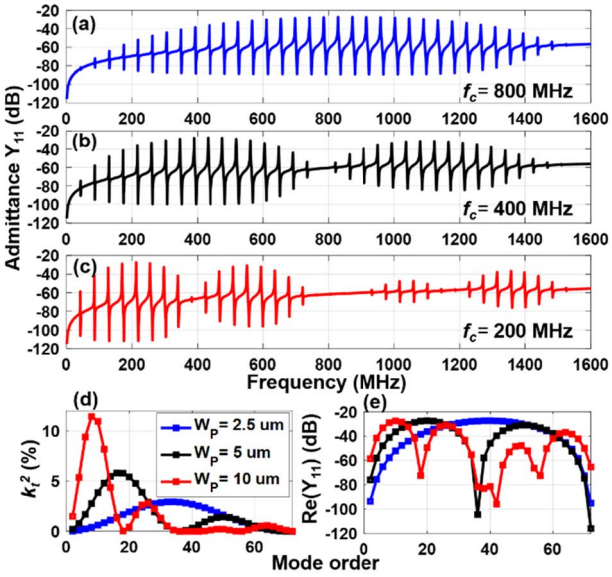

Fig. 4. Admittance of the LOBAR with (a) $W_P = 2.5$ μm, (b) $W_P = 5$ μm, and (c) $W_P = 10$ μm. (d) k_t^2 and (e) $1/R_m$ of LOBAR with $W_P = 2.5$, 5, and 10 μm. $W_T = 100$ μm, $C_o = 180$ fF, and $Q = 2000$ values are used in these simulations.

VCMO, is collectively determined by various loss mechanisms originated from the materials stack and the design. Finally, the k_t^2 distribution among different tones is modeled and shown in Fig. 2(b). Fig. 2(b) shows an excitation of 17 tones ranging from 100 to 800 MHz with a spacing of 40 MHz. The tones are centered around 400 MHz (mode order 16). This mode has the highest k_t^2 of ~6% among the 17 modes. Only 10 tones (mode orders 8–26) lie within the KBW of the resonator (the green shaded area). The first lobe in Fig. 2(b) covers mode orders from 2 to 36, corresponding to the resonances from 100 to 800 MHz in Fig. 2(a).

Section II-B focuses on optimizing the three main design parameters, namely, W_T, W_P, and the number of transducers (N_T). These parameters set the resonator specifications f_n, Δf, f_{center}, KBW, and k_t^2, which will finally determine the VCMO tuning range and the number of RF carriers generated at the output of the VCMO. The fabricated device performance will be presented in Section II-D.

B. Design Space

Investigating the design space of the LOBAR is an important step toward building the VCMO. This space can be quantified through capturing the effect of varying the main resonator parameters on the admittance profile, as shown in Figs. 3–6. By varying W_T while fixing $W_P = 5$ μm, $C_o = 180$ fF, and $Q = 2000$, the frequency spacing (Δf) can be controlled while fixing the center frequency (f_{center}) to 400 MHz, as shown in Fig. 3. Δf and k_t^2 almost get halved by doubling W_T. A smaller Δf ideally results in a wider tuning range for the VCMO; however, the ability of the oscillator to lock to a certain tone and suppress others decreases. A smaller k_t^2 as a result of a larger resonator width will increase the VCMO power consumption as shown in Fig. 3(e), where the

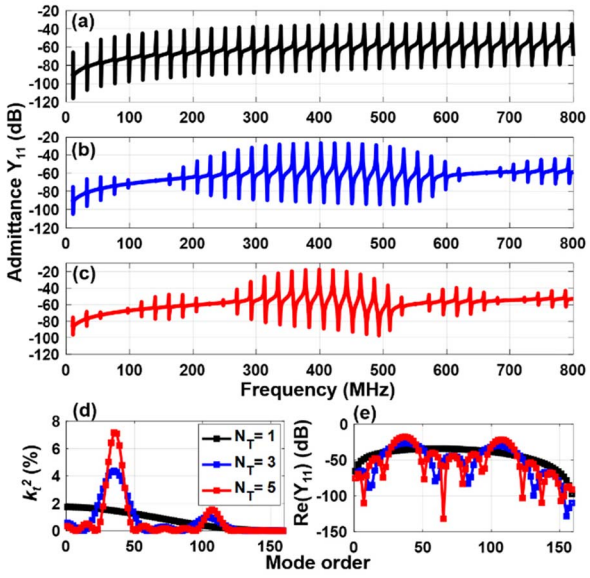

Fig. 5. Admittance of the LOBAR with (a) $N_T = 1$, (b) $N_T = 3$, and (c) $N_T = 5$. (d) k_t^2 and (e) $1/R_m$ of LOBAR with $N_T = 1$, 3, and 5. $W_T = 200$ μm, $W_P = 5$ μm, and $Q = 2000$ are used in these simulations.

real portion of the admittance ($1/R_m$) at different f_n values is plotted versus the mode orders for different W_T values. Moreover, the resonator KBW increases with an increase in W_T at the expense of a smaller k_t^2. In summary, a larger resonator width translates to a wider tuning range, lower locking stability, and higher power consumption.

On the other hand, varying W_P, while fixing $W_T = 100$ μm, $C_o = 180$ fF, and $Q = 2000$, f_{center} can be controlled while fixing Δf to 40 MHz, as shown in Fig. 4. f_{center} gets halved while k_t^2 almost double via doubling W_T. A smaller f_{center} results in a smaller frequency of oscillation. A larger k_t^2 as

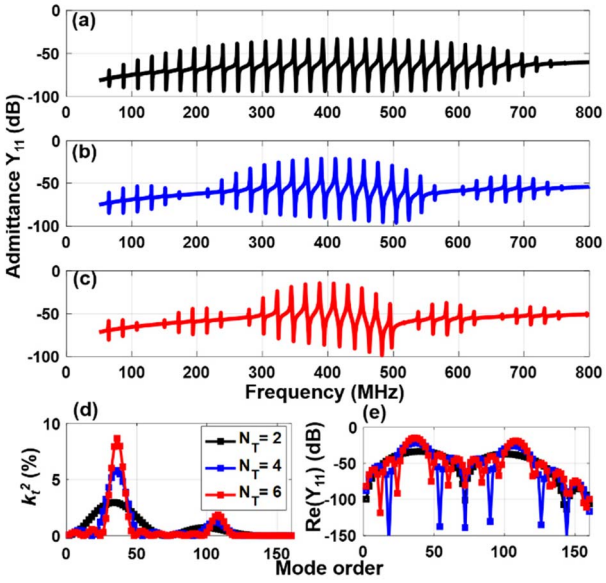

Fig. 6. Admittance of the LOBAR with (a) $N_T = 2$, (b) $N_T = 4$, and (c) $N_T = 6$. (d) k_t^2 and (e) $1/R_m$ of LOBAR with $N_T = 2$, 4, and 6. $W_T = 200\ \mu$m, $W_P = 5\ \mu$m, and $Q = 2000$ are used in these simulations.

a result of a larger resonator pitch will result in a reduction in the VCMO power consumption as shown in Fig. 4(e), where $1/R_m$ is plotted versus the mode orders for different W_P values.

Moreover, the resonator KBW and hence the VCMO tuning range decrease with an increase in W_T. To summarize, a larger resonator pitch translates to a lower oscillation frequency, a small tuning range, and less power consumption.

Following the RF synthesizer requirements, the VCMO should lock to at least ten overtones centered around 400 MHz with a tuning range of at least 200 MHz. These numbers translate to a Δf of 20 MHz and f_{center} of 400 MHz. Hence, the LOBAR should have a KBW greater than 200 MHz exciting the resonant modes characterized by the highest k_t^2 spanning between 300 and 500 MHz. According to the abovementioned specifications and (1)–(3), W_T is set to 200 μm and W_P to 5 μm. Now, the number of transducers (N_T) must be determined as the next design step to complete the LOBAR design.

Figs. 5 and 6 show the effect of N_T (N_T = no. of IDEs − 1) on the resonator performance. According to [40], even- and odd-order modes cannot be excited simultaneously in a resonator cavity with centered transducers. Only even-order modes can be excited with even numbers of centered transducers, whereas only odd-order modes can be excited with odd numbers of centered transducers. A detailed study on offsetting the transducers from the center of the resonator can be found in [40], which will allow excitation of both the odd- and even-order modes. In this article, the focus is on LOBARs with IDTs centered on the resonator cavity. Although N_T has no primary effect on setting f_{center} nor Δf, its effect on the KBW and k_t^2 should be considered. A larger N_T translates to a higher maximum k_t^2 and a smaller KBW and, hence, lower power consumption and smaller tuning range for VCMOs, respectively. Moreover, larger N_T translates to lower Q due to the increase of the metal-piezo losses. For a single transducer design, the low-pass behavior shown in Fig. 5(d) rejects the signals at higher frequencies, which is not desirable for tunable RF VCMOs where the tuning range is usually specified around a certain carrier. Moreover, Fig. 5(e) shows a much higher R_m for a single IDT when compared with three or five IDTs and thus higher power consumption. Finally, after considering the abovementioned tradeoffs, N_T of 2 is chosen in this work to achieve a maximum Q (hence, best close-in phase noise on the circuit level) and maximum tuning range at the expense of slightly higher power consumption.

C. MBVD Model

The LOBAR is modeled inside in the VCMO circuitry using the modified Butterworth–Van Dyke (MBVD) model [11]. Using this model, the input impedance to the resonator Z_{MEMS} can be expressed as follows:

$$Z_{\text{MEMS}} = \left(R_m + j\omega L_m + \frac{1}{j\omega C_m}\right) \Bigg\| \frac{1}{j\omega C_o} \approx R_m\left(1 + j\left(\frac{2Q_u(f - f_s)}{f_s}\right)\right) \Bigg\| \frac{1}{j\omega C_o} \tag{4}$$

where R_m, L_m, and C_m are the motional resistance, the motional inductance, and the motional capacitance, respectively. f_s is the series resonance frequency, Q_u is the unloaded quality factor ($Q_u = \omega L_m/R_m$), and $\omega = 2\pi f$. The parameters R_m, L_m, and C_m can be expressed in terms of independent parameters such as C_o, Q_u, f_s, and k_t^2, as shown in [11]. Solving for the resonance where Z_{MEMS} is real, f_s and the antiresonance f_p can be calculated, as shown in (5) and (6), respectively. The MBVD model has only one static branch realized by C_o in parallel to ten motional branches instead of ten static branches if those ten modes are to be realized through ten conventional resonators, each targeting a single mode

$$f_s = \frac{1}{2\pi\sqrt{L_m C_m}} \tag{5}$$

$$f_p = f_s\sqrt{1 + \frac{C_m}{C_o}}. \tag{6}$$

D. Fabricated LOBAR

Fig. 7(a) shows the measured and MBVD fitted responses of the fabricated LOBAR. The LOBAR has the following parameters: $W_T = 200\ \mu$m, $W_P = 5\ \mu$m, $N_T = 2$, and $C_o = 125$ fF. The main specs (f_n, Q, k_t^2, FOM, and R_m) of the LOBAR for the ten locked overtones spanning from 300 to 500 MHz are given in Table I. As a zoomed-in view example, the measured admittance of the 415-MHz resonance is shown in Fig. 7(b), while the optical image of the device is shown in Fig. 7(c). The device uses the same fabrication process reported in [22]. The resonator was fabricated using a transferred $LiNbO_3$ thin film on a Si carrier substrate. The resonator is composed of an 800-nm $LiNbO_3$ thin film with 250-nm Al electrodes on top. Average Qs of 2100, k_t^2 of 1.5%, FOM of 31.5, and R_m of 140 help in enabling low phase noise and low-power oscillators that are crucial for IoT.

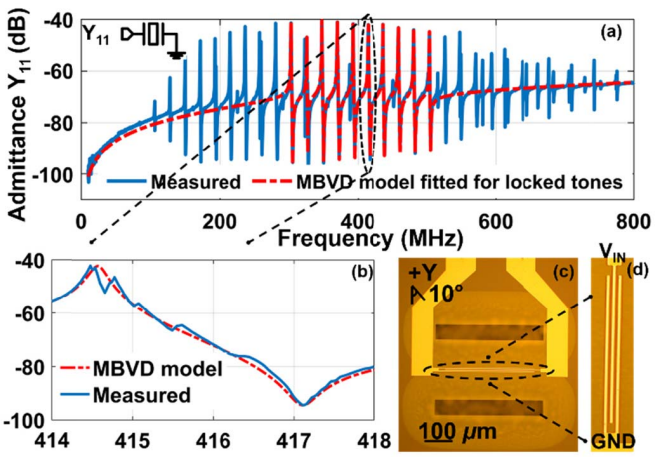

Fig. 7. (a) Measured and MBVD fit responses of the LOBAR. (b) Measurement of the 415-MHz resonance. (c) Optical image of the LOBAR. (d) Zoomed-in view of the LOBAR.

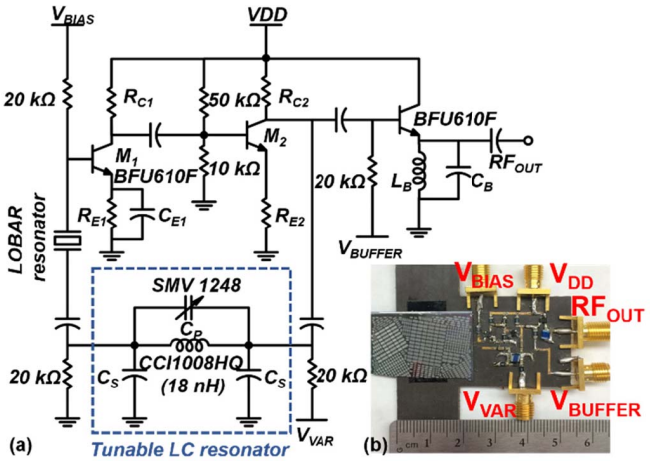

Fig. 8. (a) VCMO circuit schematic. (b) Board implementation.

TABLE I
EXTRACTED PARAMETERS OF THE TEN OVERTONES IN 300–500-MHz RANGE

Spec/Mode	1	2	3	4	5	6	7	8	9	10
f_n (MHz)	305	325	345	370	390	415	435	460	480	505
Q	1650	1671	1945	1825	1908	1970	2608	2050	2202	3000
k_t^2 (%)	2.56	1.29	2.19	2.02	1.69	1.48	1.09	1.13	0.89	0.59
FOM	42.3	21.6	42.63	36.9	32.2	29.2	28.4	23.2	19.6	17.7
R_m (Ω)	122	225	107	115	125	130	127	147	167	175
C_o (fF)	125									

In comparison to switching between lithographically defined multiple resonators, our LOBAR saves area by packing over 30 resonances in a single device rather than using 30 stand-alone resonators. Moreover, LOBARs usually have higher Q at the same frequency when compared with the conventional single-mode resonators due to the lower metallization ratio, thus improving the close-in phase noise performance.

III. RECONFIGURABLE OSCILLATOR

In this section, we first introduce the VCMO schematic and the optimization of phase noise, tuning range, and power consumption. Then, RF measurements on the $LiNbO_3$ LOBAR VCMO are presented. The VCMO is designed with the capability to lock to the maximum number of LOBAR tones centered around f_{center} (~400 MHz).

A. Overview

The oscillator in Fig. 8(a) consists of an LOBAR in a closed loop with two common-emitter degenerated amplifiers and a voltage tunable varactor-embedded LC resonator. Each of these blocks has a function inside the loop, the LOBAR excites different tones, the amplifier provides enough gain to start and sustain the oscillation, and the LC tank selects a certain overtone and suppresses others. The tunable LC tank is comprised of an inductor and a varactor in parallel and loaded by two shunt capacitors C_s to the ground. By tuning the bias voltage V_{VAR} of the varactor C_p, the LC tank adjusts the loop so that the Barkhausen conditions can be satisfied for an acoustic resonant mode excited via the LOBAR. Hence, only one oscillation frequency (f_o) is produced at the output guaranteeing a stable oscillation. A common collector buffer is used to match the output to 50 Ω needed for the measurements.

Section III will focus on the design and analysis of the LOBAR VCMO, and several specifications will be considered in our analysis such as tuning range, power consumption, and phase noise.

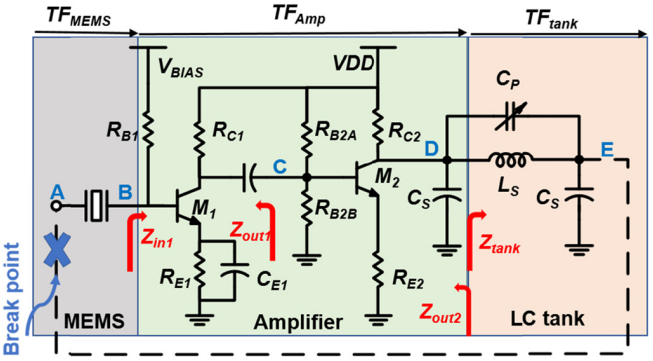

Fig. 9. Breaking the loop at point *A*. This figure also shows the three main components of our VCMO.

B. Transfer Functions

To fully understand the VCMO, several transfer functions (TFs) are developed. These functions characterize the gain or the loss of the circuit. To this end, we will divide the oscillator loop into three segments as shown in Fig. 9 and derive the TF for each segment. We break the loop at Point *A* shown in Fig. 9 while paying attention to the loading of the circuitry.

1) Amplifier: The two degenerated common-emitter stages have a combined gain of TF_{Amp} which is defined as the voltage at node D divided by the voltage at node B, as shown in Fig. 9.

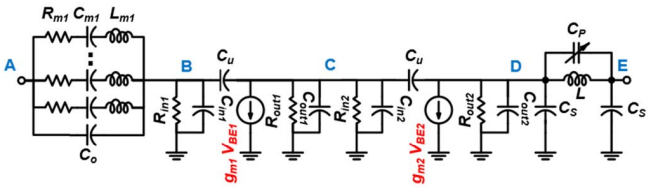

Fig. 10. Small-signal model of the VCMO.

$\mathrm{TF_{Amp}}$ is derived as follows:

$$\mathrm{TF_{Amp}} = \mathrm{TF_{Amp1}}\mathrm{TF_{Amp2}} = G_{m1}Z_{\mathrm{out1}}G_{m2}Z_{\mathrm{out2}} \tag{7}$$

where G_{m1} and G_{m2} are the degenerated transconductances of the first and second stages and Z_{out1} and Z_{out2} are the output impedances of the first and second stages, respectively. They are given in the following equations as functions of the small-signal circuit parameters shown in Fig. 10:

$$G_{m1} = \left(\frac{g_{m1}}{1+\left|\frac{g_{m1}R_{E1}}{1+sR_{E1}C_{E1}}\right|}\right) \tag{8}$$

$$Z_{\mathrm{out1}} = \left(\frac{R_{\mathrm{out1}}\|R_{\mathrm{in2}}}{1+s(R_{\mathrm{out1}}\|R_{\mathrm{in2}})(C_{\mathrm{out1}}+C_{\mathrm{in2}})}\right) \tag{9}$$

$$G_{m2} = \left(\frac{g_{m2}}{1+g_{m2}R_{E2}}\right) \tag{10}$$

$$Z_{\mathrm{out2}} = \left(\frac{R_{\mathrm{out2}}}{1+sR_{\mathrm{out2}}(C_{\mathrm{out2}}+C_S)}\right)\Bigg\|Z_{\mathrm{tank}} \tag{11}$$

where $C_{\mathrm{out1}} = C_{o1} + C_\mu$, and $C_{\mathrm{in2}} = C_{i2} + C_\mu(1 + g_{m2}R_{\mathrm{out2}})$. C_{o1} is the parasitic capacitance at the collector of M1, C_{i2} is the parasitic capacitance at the base of M2, and C_μ is the parasitic capacitance between the base and collector of M1 or M2. $s = j\omega$ and $g_{m1} = I_{C1}/(KT/q)$. R_{out1} is given as

$$R_{\mathrm{out1}} = R_{C1}\|[R_{x1} + r_{o1}(1 + g_{m1}R_{x1})] \tag{12}$$

$$R_{x1} = R_{E1}\|(r_{\pi 1} + r_b) \tag{13}$$

$$R_{\mathrm{in2}} = R_{B2}\left\|\left(r_{\pi 2} + r_b + \frac{R_{E2}(1+\beta_o)\left(r_{o2}+\frac{R_{C2}}{1+\beta_o}\right)}{r_{o2}+R_{C2}+R_{E2}}\right)\right. \tag{14}$$

$$Z_{\mathrm{tank}} = \left(\frac{r_s + sL}{1 + sr_sC_P + s^2LC_P}\right) + \frac{1}{sC_s} \tag{15}$$

where $R_{B2} = R_{B2\,A}\|R_{B2\,B}$, $r_{\pi 1} = \beta_o/g_{m1}$, r_{o2} is early voltage/I_{C2}, r_b is the base series resistance, and β_o is the small-signal current gain. $r_s = \omega L/Q_{\mathrm{tank}}$, with L the tank inductance, Q_{tank} the tank coil quality factor, C_p the tank varactor, and C_s the tank capacitive load. R_{out2} equation is the same as R_{out1} but using subscript 2 instead of 1 and the same for $r_{\pi 2}$, R_{in2}, and C_{out2}. Equation (7) is shown along with a circuit simulation in Fig. 11(a). The equation matches perfectly the circuit simulations.

For the amplifier, the design aims to provide enough loop gain $\mathrm{TF_{Amp}}$ to satisfy the Barkhausen conditions with minimum noise added to the loop and lowest power consumption. Silicon germanium BFU610F is chosen as the transistors for its low noise figure and low power consumption. V_{BE} bias voltages of M1 and M2 are chosen based on three factors: first, a small BJT base current (I_B) that gives a low flicker noise; second, a reasonable gain for a single resonance without satisfying Barkhausen conditions for any other tones, especially when the tones are very close with a Δf of 20 MHz; and third, low power consumption. The buffer design is borrowed from the millimeter-wave regime, where the VCO buffers use a quarter wavelength stub to cancel the imaginary output impedance and match the real output impedance ($1/g_m$) of the buffer emitter to 50 Ω. For lower frequency designs, an LC tank can be used to have the same effect as the stub. The tank reduces the power consumption in the buffer for the same output power when compared with a resistive loading.

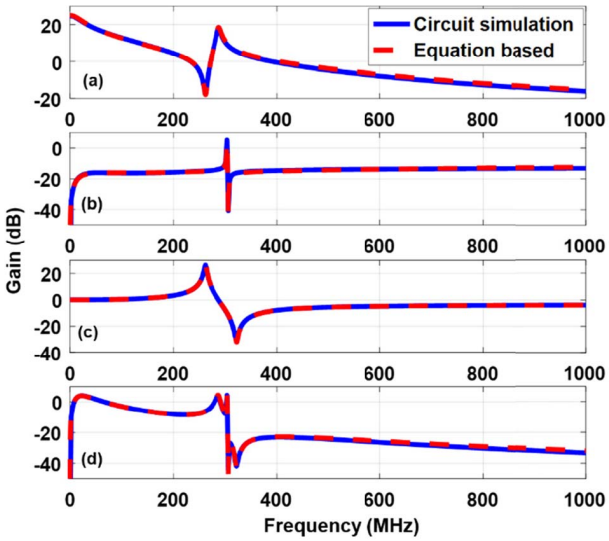

Fig. 11. Circuit simulations and equation-based TFs of different components in the VCMO. (a) $\mathrm{TF_{Amp}}$, (b) $\mathrm{TF_{MEMS}}$, (c) $\mathrm{TF_{tank}}$, and (d) $\mathrm{TF_{loop}}$. Equations and simulations match perfectly. Parameters used in these simulations: $g_{m1} = 11.9$ mS, $g_{m2} = 6.4$ mS, $R_{\mathrm{out}} = 1.98$ kΩ, $R_{\mathrm{out2}} = 510$ Ω, $R_{\mathrm{in1}} = 10$ kΩ, $R_{\mathrm{in2}} = 7$ kΩ, $R_m = 122$ Ω, $C_m = 2.6$ fF, $L_m = 106.05$ μH, $C_s = 7$ pF, and $C_p = 13.5$ pF. Only one LOBAR overtone (300 MHz) is shown in the plot for figure clarity.

2) LOBAR: The LOBAR admittance profile and MBVD model are presented in Section I. Z_{MEMS} derived in (4) is the voltage across the resonator divided by the current through it. Here, we define $\mathrm{TF_{MEMS}} = V_B/V_A$, taking into consideration the loading of the amplifier on the LOBAR. $\mathrm{TF_{MEMS}}$ is shown in Fig. 11(b) for only the 300-MHz tone and is given as

$$\mathrm{TF_{MEMS}} = \frac{Z_{\mathrm{in1}}}{Z_{\mathrm{in1}} + Z_{\mathrm{MEMS}}} \tag{16}$$

where Z_{in1} is given as

$$Z_{\mathrm{in1}} = \left(\frac{R_{\mathrm{in1}}}{1+sR_{\mathrm{in1}}C_{i1}}\right)\Bigg\|\left(\frac{\frac{R_{\mathrm{out1}}}{1+sR_{\mathrm{out1}}C_{\mathrm{out1}}} + \frac{1}{sc_u}}{1+G_{m1}\frac{R_{\mathrm{out1}}}{1+sR_{\mathrm{out1}}C_{\mathrm{out1}}}}\right). \tag{17}$$

3) LC Tank: A CCI1008HQ inductor of 18 nH is chosen as the tank inductor. This value allows for locking to the LOBAR resonances with the lowest R_m in the range of 300–500 MHz. The inductor has a minimum Q_{tank} of 62 at 350 MHz, a minimum self-resonant frequency (SRF) of 2.7 GHz, and a maximum DCR of 0.07 Ω. For the LC tank, $\mathrm{TF_{tank}} = V_E/V_D$

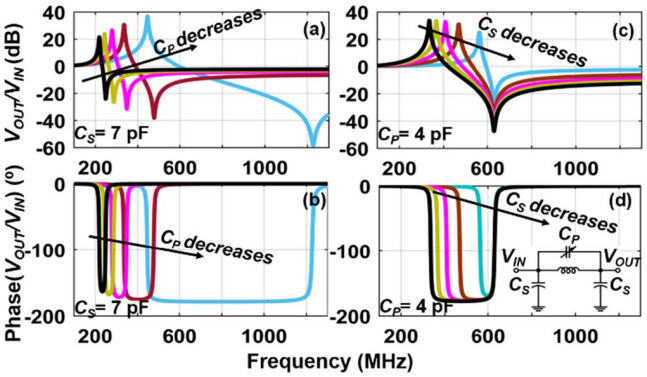

Fig. 12. (a) Gain and (b) phase responses with C_s fixed to 7 pF and C_p varying from 1 to 25 pF. (c) Gain and (d) phase responses with C_p fixed to 4 pF and C_s varying from 1 to 10 pF.

is given as follows and shown in Fig. 11(c):

$$\mathrm{TF}_{\mathrm{tank}} = \frac{1}{sC_s\left(\frac{r_s+sL}{1+sr_sC_P+s^2LC_P}\right)+1}. \tag{18}$$

As deduced from (18), the tank has both series (f_s^t) and parallel resonances (f_p^t). Controlling these frequencies will be discussed in Section III-C. Both frequencies are given as follows:

$$f_s^t = \frac{1}{2\pi\sqrt{L\left(C_s+C_p\right)}} \tag{19}$$

$$f_p^t = \frac{1}{2\pi\sqrt{LC_p}}. \tag{20}$$

Finally, the loop gain $\mathrm{TF}_{\mathrm{loop}}$ is shown in Fig. 11(d) and given as

$$\mathrm{TF}_{\mathrm{loop}} = \mathrm{TF}_{\mathrm{Amp}}\mathrm{TF}_{\mathrm{MEMS}}\mathrm{TF}_{\mathrm{tank}} \tag{21}$$

where the multiplication of $\mathrm{TF}_{\mathrm{MEMS}}$ and $\mathrm{TF}_{\mathrm{tank}}$ will be referred to as β_{loop}. By satisfying abs ($\mathrm{TF}_{\mathrm{loop}}$) $>$ 1 and solving for Imag ($\mathrm{TF}_{\mathrm{loop}}$) $= 0$, the VCMO oscillation frequency (f_o) is calculated. The parameters used to generate Fig. 11 are given as follows: $g_{m1} = 11.9$ mS, $g_{m2} = 6.4$ mS, $R_{\mathrm{out1}} = 1.98$ kΩ, $R_{\mathrm{out2}} = 510$ Ω, $R_{\mathrm{in1}} = 10$ kΩ, $R_{\mathrm{in2}} = 7$ kΩ, $R_m = 122$ Ω, $C_m = 2.6$ fF, $L_m = 106.05$ μH, $C_s = 7$ pF, and $C_p = 13.5$ pF. The equations for different TFs are derived in (7)–(21), and these TFs will serve as an introduction to fully explore the design space of the VCMO analytically in Section III-C.

C. Locking Mechanism

Design choices related to the LC tank, such as C_s, C_p, and Q_{tank}, and others related to the LOBAR, such as k_t^2 and C_o, need to be investigated. The effects of C_s and C_p on the tank TF are shown in Fig. 12. C_s controls only f_s^t given in (19), whereas C_p controls both f_s^t and f_p^t given in (20). A smaller C_s leads to higher f_s^t and smaller tank inductive range, i.e., bandwidth (BW $= f_p^t - f_s^t$), hence affecting fewer overtones. On the other hand, a smaller C_p leads to the larger spacing between both resonant frequencies and larger BW, thus affecting more overtones. Since C_s does not have control

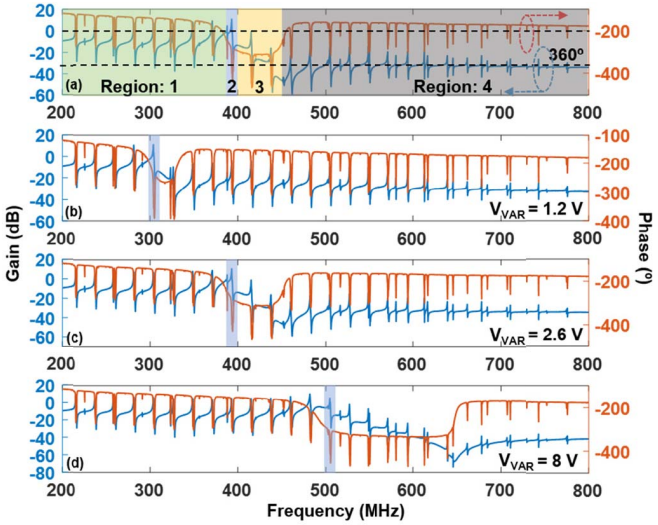

Fig. 13. (a) Illustration of four regions. (b)–(d) Simulated loop gain and loop phase response for three different varactor bias voltages spanning the tuning range. Only three voltages are represented instead of ten for figure clarity. The measured S-parameters of the LOBAR are used in these simulations.

over the position of f_p^t as shown in Fig. 12(c) while C_p does, C_s is chosen to be fixed in the implementation and an SMV1248 varactor is chosen to implement C_p that can be varied from 22.62 to 1.3 pF as V_{VAR} varies from 0 to 8 V.

The spectrum can be divided into four regions with respect to f_s^t and f_p^t, as shown in Fig. 13(a). In Region 1 where frequencies are lower than f_s^t, the overtones fulfill the gain condition of oscillation but do not fulfill the phase condition. In Region 2 where the frequency aligns with f_s, the tone is coupled with a maximum gain. Furthermore, in Region 3 where frequencies lie within the tank BW closer to f_p^t, the tones get suppressed in gain despite fulfilling the phase condition. Finally, in Region 4 where frequencies are larger than f_p^t, the overtones do not fulfill both the gain and phase conditions. Therefore, the targeted LOBAR tone should be as close as possible to f_s^t inside the tank inductive region. Fig. 13(b)–(d) shows the simulated loop gain and phase response of the VCMO for three different varactor bias voltages spanning the tuning range.

As previously mentioned, the LC tank selects the targeted resonance to be amplified inside the oscillator, creating a stable RF carrier and suppressing other LOBAR modes. Hence, the suppression of the nearby tones and the oscillation stability depend on the value of Q_{tank}. Moreover, the loop phase and loop gain $\mathrm{TF}_{\mathrm{loop}}$ at the targeted resonance, and thus the power consumption, depends on Q_{tank}. A study showing the effect of Q_{tank} on $\mathrm{TF}_{\mathrm{loop}}$ is shown in Fig. 14. A larger Q_{tank} translates to a higher loop gain for the targeted LOBAR resonance and a larger suppression of the nearby modes. For instance, one can target the 300-MHz mode by setting V_{VAR} to 1.2 V, as shown in Fig. 14(a) and (b). As a result, $\mathrm{TF}_{\mathrm{loop}}$ increases by 5 dB and the suppression of the nearest unwanted mode ($\mathrm{TF}_{\mathrm{loop|300\ MHz}} - \mathrm{TF}_{\mathrm{loop|320\ MHz}}$) increases by 7.6 dB as Q_{tank} increases from 10 to 75. Moreover, the phase dip increases by ∼40°, providing enough margin for phase

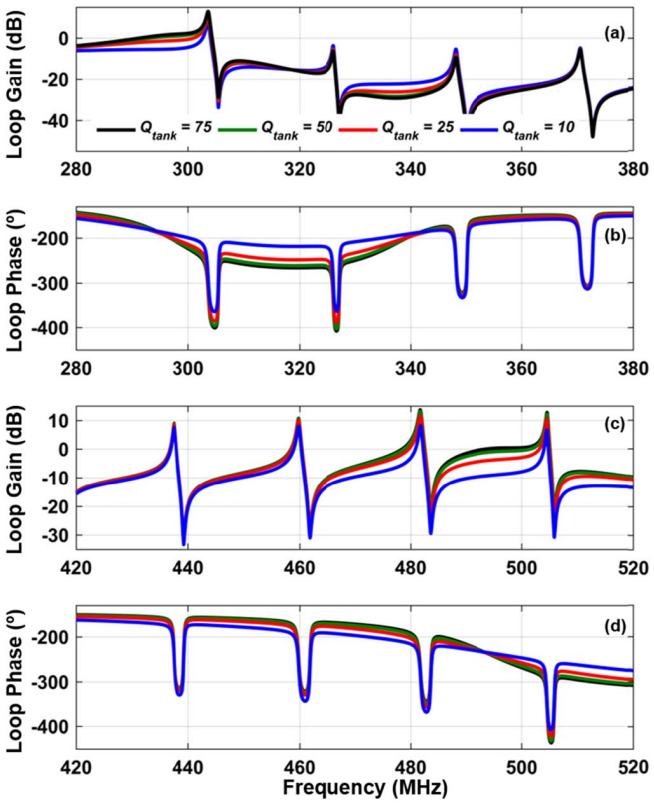

Fig. 14. Effect of Q_{tank} on the simulated loop gain and loop phase. (a) and (b) $V_{\text{VAR}} = 1.2$ V. (c) and (d) $V_{\text{VAR}} = 8$ V. Q_{tank} is varied from 10 to 75. The LOBAR MBVD model is used in these simulations rather than measured S-parameters for figure clarity.

shift and more stable oscillation. The 500-MHz resonance is excited by setting V_{VAR} to 8 V, as shown in Fig. 14(c) and (d). TF_{loop} increases by 6 dB and the suppression of the nearest unwanted mode ($\text{TF}_{\text{loop|505 MHz}} - \text{TF}_{\text{loop|480 MHz}}$) increases by 4.7 dB as Q_{tank} increases from 10 to 75. Moreover, the phase dip increases by ∼28° at 505 MHz providing enough margin for phase shifts and more stable oscillation. A Q_{tank} below 25 permits satisfying the Barkhausen conditions of oscillation for more than one mode, thus making it undesirable for our application. For instance, a Q_{tank} of 10 increases the phase dip for the 480-MHz resonance by ∼24°, consequently allowing oscillations at both the 480- and 505-MHz resonances.

This Q_{tank} study also sheds some light on the applicability of implementing LOBAR VCMOs on CMOS. CMOS offers on-chip inductors with low Qs, hence affecting the design choices of the LOBAR itself. Larger frequency spacing (Δf) between the modes might be needed for stable oscillations with CMOS. A larger Δf can be easily achieved using a smaller device width W_T, as discussed previously in Section II-B.

D. C_o and k_t^2 of LOBAR

Continuing with the idea of codesigning the mechanical and electrical portions of our system, investigating the effect of C_o and k_t^2 is crucial for building the largest tuning range, lowest power consumption, and best phase noise MEMS oscillator. Revisiting Section II-C, R_m is inversely proportional to f_s, Q, C_o, and k_t^2, while C_o is set by the size of the IDTs. Hence, both parameters heavily depend on W_T, W_P, and N_T mentioned earlier. By fixing k_t^2, f_s, and Q (through fixing W_T, W_P, and N_T) and increasing C_o (via increasing the lengths of the IDTs), the MBVD model should be adjusted by increasing C_m and decreasing both L_m and R_m with the same ratio of increasing C_o. Fig. 15(a) shows the effect of increasing C_o on TF_{loop}. Take the 300-MHz resonance for instance, the loop gain increases by 2 dB with an increase in C_o from 50 to 150 fF, as shown in Fig. 15(a). This is from a three times smaller R_m. The phase dip is minimally affected by C_o variations. Larger loop gain translates to lower power consumption and better far-from-carrier phase noise.

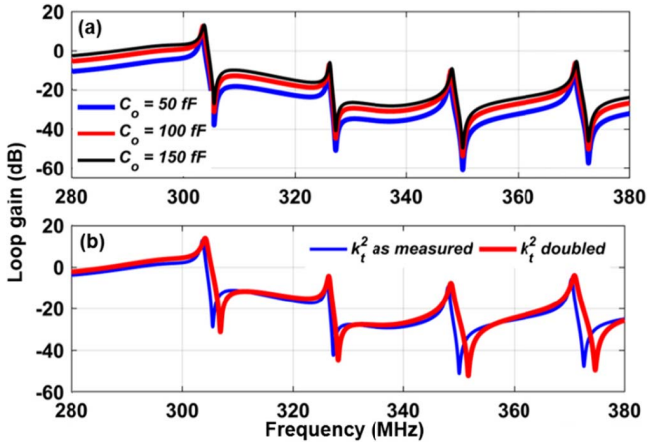

Fig. 15. (a) Effect of increasing C_o from 50 to 150 fF in three steps. (b) Effect of doubling k_t^2. $V_{\text{VAR}} = 1.2$ V.

A study on varying k_t^2 while fixing Q, f_s, and C_o was also considered. Fig. 15(b) shows the effect of doubling k_t^2 on the loop gain. For the 300-MHz resonance, loop gain increases by 1 dB, phase dip increases by 10°, and the BW of each tone ($f_p - f_s$) increases by ∼50%, which is beneficial for fine-tuning the oscillation frequency within the BW of the tone by fine adjusting the varactor bias V_{VAR}. Fine-tuning might be helpful to overcome environmental or temperature frequency shifts. After analyzing the effect of the LOBAR and LC tank parameters on the loop TFs, the next step is to analyze the phase noise of our LOBAR VCMO.

E. Phase Noise

The phase noise analysis herein is based on the linear time-invariant (LTI) classical theory [43]–[45] that predicts the oscillator phase noise given in (22). The derivation can be found in [45]

$$L(f_m) = 10\log_{10}\left[\frac{kTF}{2P_s}\left(1+\frac{f_c}{f_m}\right)|G_{\text{noise}}(f_m)|^2\right] \quad (22)$$

where k is Boltzmann's constant, T is the temperature in kelvin, F is the amplifier noise factor, P_s is the carrier power at the amplifier output, f_c is the flicker noise corner, f_m is the offset frequency from the oscillator carrier frequency f_o (i.e., $f_m = f - f_o$) where the PSD is calculated, and $G_{\text{noise,ideal}}$

is the closed-loop noise TF for an ideal loop is given as

$$G_{\text{noise,ideal}}(f_m) = \frac{1}{1 - H_{\text{ideal}}(f_m)} \tag{23}$$

where $H_{\text{ideal}}(f_m)$ is the TF of an ideal resonator assuming a small R_m, neglecting C_o and an ideal closed loop with no loading on the resonator, and H_{ideal} can be calculated as

$$H_{\text{ideal}} \sim \frac{1}{1 + j\left(\frac{2Qf_m}{f_o}\right)} \tag{24}$$

which is the inverse of (4) neglecting R_m and C_o. Here, the carrier frequency f_o is assumed to be equal to the resonant frequency f_s given in (5) for a high Q resonance. By substituting (24) into (22), we can have Leeson's phase noise formula [45]

$$L(f_m) = 10\log_{10}\left[\frac{kTF}{2P_s}\left(1 + \frac{f_c}{f_m}\right)\left(1 + \left(\frac{f_o}{2Qf_m}\right)^2\right)\right]. \tag{25}$$

Phase noise negatively affects wireless communications. The close-to-carrier noise adds directly to the system noise figure by adding noise inside the system bandwidth, whereas the far-from-carrier noise weakens the ability of a receiver to attenuate undesired adjacent channel signals. Both should be reduced in a good oscillator design. Equation (25) expresses the four major causes of noise, the upconverted $1/f$ noise (flicker FM noise with f_m^{-3} slope), the thermal FM noise (with f_m^{-2} slope), the flicker phase noise (with f_m^{-1} slope), and the thermal noise floor with constant PSD. For high Q oscillators such as MEMS oscillators, $f_o/2Q$ is usually a lower frequency than f_c for most of the transistor technologies and megahertz carrier frequencies, resulting in masking the f_m^{-2} region in the phase noise profile [44]. Each region of the phase noise curve brings different design challenges. For the noise floor, we want to dissipate as much power in the motional branch ($P_m = R_m I_m^2$) of the resonator as long as it operates in the linear regime (larger P_m reduces far-from-carrier phase noise). This can be guaranteed if most of the ac current passes through the motional arm at resonance (R_m) rather than the static arm (C_o) inside the resonator. Yet, the oscillator should consume low power for IoT applications, hence leading to the well-known phase noise and power consumption tradeoff. The oscillator core must be designed to remain in a low noise operation (low noise factor F) for the design point of the resonator. In the close-to-carrier region, the main factor in determining the phase noise of the oscillator is the loaded Q of the resonator Q_L. The phase noise in this region is mainly due to the upconversion of $1/f$ flicker noise of the amplifier. The oscillator core bias point, the bias circuit design, and the transistor flicker noise are all significant contributors to the oscillator noise. Finally, the phase noise in the intermediate region is ruled by the upconversion of the thermal noise.

The abovementioned analysis is general for any oscillator. In Sections III-E1 and III-E2, we will perform phase noise analysis more specifically to our LOBAR oscillator. The goal is to find all the unknown parameters in (22), such as G_{noise}, F, and f_c, relating the LOBAR VCMO circuit parameters and the circuit loading effects on the resonator. P_s will be treated as a given value since the oscillator output power is usually given for an oscillator.

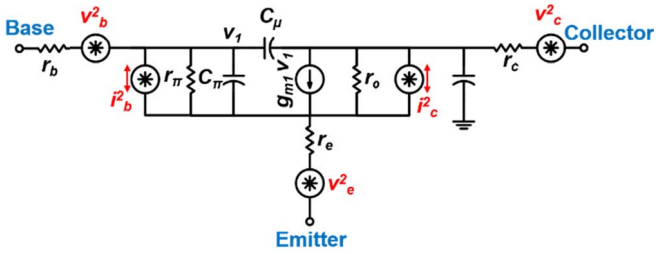

Fig. 16. BJT small-signal model with noise sources.

1) Amplifier Noise Factor F and Flicker Corner f_c: To find F, we start by identifying the noise sources in our VCMO. Generally, the noise sources for a MEMS oscillator can be divided into two groups, electronic and mechanical noise sources. Electronic noise sources include thermal and flicker noises of the active and passive devices used in the VCMO and these are the focus of this section. The low-frequency mechanical noise in the resonator originates from two sources: the nonlinearity of the micromechanical resonator and the random low-frequency vibrations. The resonator can be driven into nonlinearity by pumping power beyond its power handling capability. Mechanical noise sources are neglected in the coming analysis as their effect on the oscillator phase noise is much lower when compared with electronic noise. The main noise sources of a BJT are shown in Fig. 16 and their TFs can be derived as follows for the amplifier:

$$\upsilon_{n,r_{b1}} = \sqrt{4KTr_b}\left|\text{TF}_{\text{Amp}}\right|, \quad \upsilon_{n,r_{b2}} = \sqrt{4KTr_b}\left|\text{TF}_{\text{Amp2}}\right| \tag{26}$$

$$\upsilon_{n,R_{E1}} = \sqrt{4KTR_{E1}}\left|\text{TF}_{\text{Amp}}\right|, \quad \upsilon_{n,R_{E2}} = \sqrt{4KTR_{E2}}\left|\text{TF}_{\text{Amp2}}\right| \tag{27}$$

$$\begin{aligned}
\upsilon_{n,R_{C1}} &= \sqrt{4KT\left|\frac{1}{1 + sR_{C1}(C_{\text{out1}} + C_{\text{in2}})}\right|}\left|\text{TF}_{\text{Amp2}}\right| \\
\upsilon_{n,R_{C2}} &= \sqrt{4KT\left|\frac{1}{1 + sR_{C2}C_{\text{out2}}}\right|}
\end{aligned} \tag{28}$$

$$\begin{aligned}
\upsilon_{n,ib_1} &= \sqrt{2qi_{b1} + \left(KFi_{b1}^{\text{AF}}\frac{1}{f^{\text{BF}}}\right)r_b}\left|\text{TF}_{\text{Amp}}\right| \\
\upsilon_{n,ib_2} &= \sqrt{2qi_{b2} + \left(KFi_{b2}^{\text{AF}}\frac{1}{f^{\text{BF}}}\right)r_b}\left|\text{TF}_{\text{Amp2}}\right|
\end{aligned} \tag{29}$$

$$\begin{aligned}
\upsilon_{n,ic_1} &= \sqrt{2qi_{c1}}\left|\frac{\left(\frac{R_{C1}}{1+g_{m1}R_{E1}}\right)}{1 + s\left(\frac{R_{C1}}{1+g_{m1}R_{E1}}\right)C_{\text{out1}}}\right|\left|\text{TF}_{\text{Amp2}}\right| \\
\upsilon_{n,ic_2} &= \sqrt{2qi_{c2}}\left|\frac{\left(\frac{R_{C2}}{1+g_{m2}R_{E2}}\right)}{1 + s\left(\frac{R_{C2}}{1+g_{m2}R_{E2}}\right)C_{\text{out2}}}\right|
\end{aligned} \tag{30}$$

$$\upsilon_{n,A1} = \sqrt{\upsilon_{n,r_{b1}}^2 + \upsilon_{n,R_{E1}}^2 + \upsilon_{n,R_{C1}}^2 + \upsilon_{n,ib_1}^2 + \upsilon_{n,ic_1}^2}$$

$$\upsilon_{n,A2} = \sqrt{\upsilon_{n,r_{b2}}^2 + \upsilon_{n,R_{E2}}^2 + \upsilon_{n,R_{C2}}^2 + \upsilon_{n,ib_2}^2 + \upsilon_{n,ic_2}^2} \tag{31}$$

$$\upsilon_{n,Amp} = \sqrt{\upsilon_{n,A1}^2 + \upsilon_{n,A2}^2} \tag{32}$$

where υ_{n,r_b}, υ_{n,R_E}, and υ_{n,R_C} are the thermal noises from the base, emitter and collector resistances, respectively. $\upsilon_{n,ib}$, and $\upsilon_{n,ic}$ are the base shot noise + flicker noise and the collector

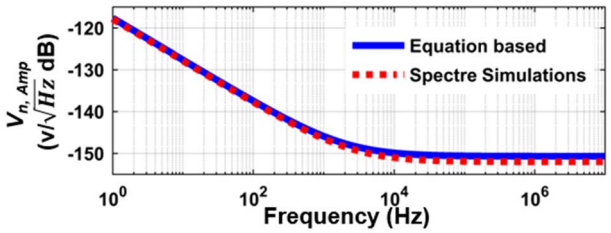

Fig. 17. Amplifier output noise based on (32) and circuit simulations.

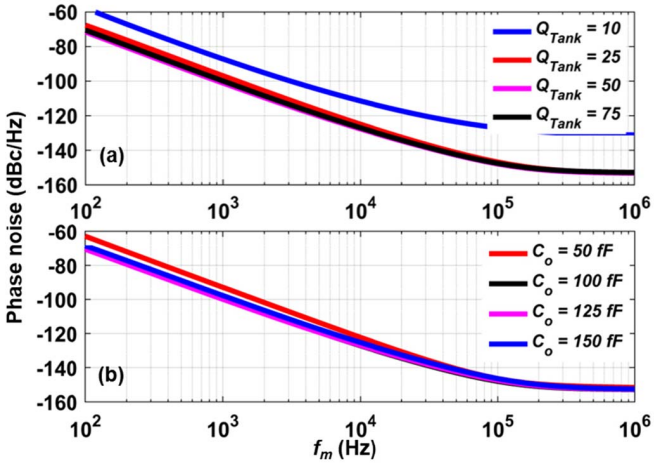

Fig. 18. Simulated effect of (a) Q_{tank} and (b) C_o on the phase noise profile of the 415-MHz carrier.

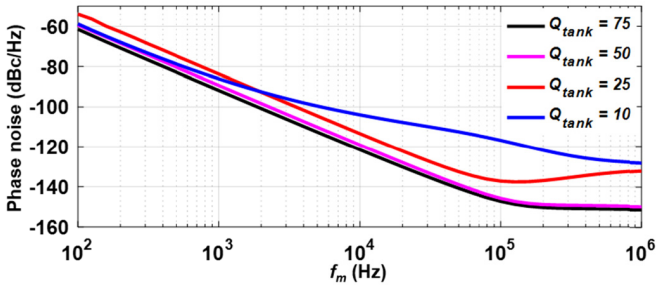

Fig. 19. Simulated effect of Q_{tank} on the phase noise profile of the 505-MHz carrier.

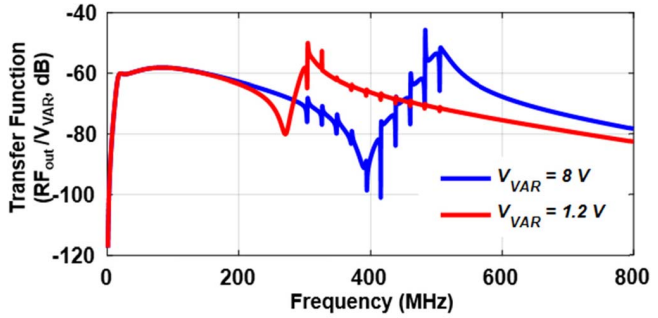

Fig. 20. TF from the varactor input (V_{VAR}) to the oscillator output (RF_{OUT}).

shot noise, respectively. KF, AF, and BF are model parameters for the flicker noise of the amplifier. In the abovementioned analysis, the noise of R_{B1} and R_{B2} is neglected due to their small effect on the overall noise in good oscillator design. Fig. 17 shows the good correlation between the simulations and (32) with a 1-dB difference in noise floors. Fig. 17 shows the generated assuming certain values for the flicker parameters (KF, AF, and BF) since they were not modeled for the transistor. These parameters were extracted from a simple curve fitting of the measured oscillator phase noise in the lab. Hence, f_c and F were extracted and fed back to (22).

2) Closed-Loop TF Gnoise Including Loading Effect: The remaining unknown parameter in (22) is G_{noise}. Considering all the parasitics and the loading effects on the LOBAR, G_{noise} is given as

$$G_{\text{noise}} = \frac{\text{TF}_{\text{Amp}}}{1 - \text{TF}_{\text{Amp}}\text{TF}_{\text{MEMS}}\text{TF}_{\text{tank}}}. \tag{33}$$

By substituting (33) into (22), we have a modified Leeson's equation for our VCMO.

3) Effect of Q_{tank} and C_o on Phase Noise: Following the same approach as Section III-C, phase noise should be investigated as a function of critical circuit parameters. Fig. 18(a) shows the effect of varying Q_{tank} on the 415-MHz resonance phase noise. The mode is excited using a simulated V_{VAR} of 3 V. Increasing Q_{tank} from 25 to 75 enhances the 1-kHz offset phase noise by 4.2 dB due to the lower loading on the LOBAR. A Q_{tank} of 10 shows a completely different phase noise profile when compared with the rest. A very low Q_{tank} deteriorates the noise floor by 23 dB due to the lower carrier power which is a result of a lower loop gain provided for such resonance as explained in Section III-C and deteriorates the 1-kHz offset noise by 14 dB when compared with a Q_{tank} of 75. The effect of increasing C_o on the phase noise profile is shown in Fig. 18(b). Increasing C_o while fixing other parameters, such as f_s, Q, and k_t^2, reduces R_m with the same ratio of increasing C_o, as previously mentioned in Section III-D. An optimal combination of C_o and R_m produces the optimum phase noise. For the 415-MHz resonance as an example, there is a sweet point at C_o of 125 fF. A very small resonator hurts the phase noise in general due to larger R_m at resonance and hence smaller carrier power.

Fig. 19 shows the effect of varying Q_{tank} on the phase noise of the 505-MHz carrier (the mode with the lowest FOM). Increasing Q_{tank} from 25 to 75 enhances the 1-kHz offset noise by 7 dB due to the lower loading on the LOBAR. A Q_{tank} of 10 shows a completely different phase noise profile in comparison to the rest, suggesting the excitement of a close-by mode (480-MHz resonance in this case, as mentioned earlier) when compared with the case with a Q_{tank} of 75. A low Q_{tank} of 10 deteriorates the 1-kHz offset noise by 5 dB and the noise floor by 23 dB due to the lower carrier power resulting from a lower loop gain provided for such resonance.

Understanding the effect of the noise at the varactor input on the phase noise profile is critical. Fig. 20 shows the TF from V_{VAR} to the oscillator output. High Q passive components and the high Q varactor used in the demonstration give a minimum noise suppression of 45 dB at 480 MHz at the varactor input.

TABLE II
PERFORMANCE SUMMARY AND COMPARISON TO RECONFIGURABLE MEMS OSCILLATORS

Reference		**This work**	[25]				[27]				[29]		[30]		[46]		
MEMS		**$LiNbO_3$ LOBAR**	AlN CMR				AlN CMR				AlN CMR		AlN-on-Si		SAW		
Process		**Discrete**	0.5 μm CMOS				0.5 μm CMOS				0.5 μm CMOS		0.5 μm CMOS		0.18 μm CMOS		
General-purpose		**Yes**	Yes				Yes				No		No		Yes		
Number of resonances		**10**	4				4				2		2		3		
Number of resonators		**1**	4				4				1		1		3		
Frequencies (MHz)		**300 - 500 (ten equally-spaced tones)**	268	483	690	785	176	222	307	482	472	1940	35	175	315	433	500
dc power (mW)		**9**	As high as 35.5				10				-	20	3.8	13.5	11.3	8.1	6.8
Output power (dBm)		**0**	1.1	0	-2.7	-6	-4.7	-4.8	-6.7	-13.6	-6.5	-16	12.1	3.8	-	-	-
PN (dBc/Hz)	1 kHz	**-100**	-94	-88	-83	-70	-79	-88	-84	-68	-82	-69	-112	-103	-	-	-
		-149.5	-142.6	-141.7	-139.8	-127.9	-123.9	-134.9	-133.7	-121.66	-135.5	-134.8	-142.9	-147.9	-	-	-
	1 MHz	**-153**	-	-	-	-	-	-160	-	-	-160	-153	-142	-140	-134	-141	-135
		-202.54						-206.9			-213.5	-218.8	-172.9	-184.9	-184	-193.8	-189
FOM_{OSC} (dBc/Hz)	1 kHz	**200**	187	186	184	172	174	185	184	172	-	182	197	197	-	-	-
	1 MHz	**193**	-	-	-	-	-	197	-	-	-	205.7	167	173.6	173.4	184.6	180.6

The values in the shaded cells are referenced to a 1 MHz carrier.

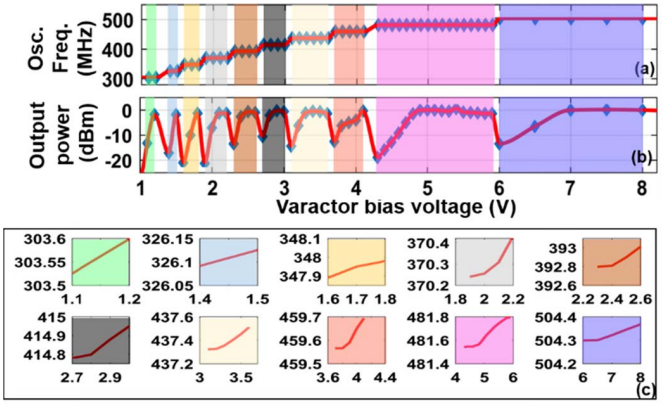

Fig. 21. (a) Oscillation frequency and (b) output power versus varactor bias. (c) Tuning response for each mode. Color codes are included for easy correlation.

This suppression translates to −105 dBc/Hz phase noise contribution from the varactor input at 1-kHz offset from a 500-MHz carrier, suppressing up to 2-$\mu V_{rms}/\sqrt{Hz}$ noise density or ∼2 mV_{rms} integrated noise up to 1-MHz bandwidth at the varactor input without affecting the phase noise values.

IV. VCMO MEASUREMENTS

SMA connectors are used for all dc biases to minimize any noise pickup from the external sources. Fig. 8(b) shows a printed circuit board (PCB) prototype with $LiNbO_3$ LOBAR sample bond-wired to the oscillator. A tunable oscillation frequency ranging from 300 to 500 MHz has been achieved by exploiting the ten overtones in the LOBAR. As shown in Fig. 21(a), the VCMO shows the continuous tuning near the series resonance of each overtone and a discrete hop of roughly 20 MHz when switching to an adjacent overtone. The continuous tuning region for each varactor bias V_{VAR} is shown in Fig. 21(c). Such a continuous range can be helpful for environmental and temperature shift corrections. This range can be increased by increasing k_t^2 of each tone and increasing the power consumption of the VCMO. As shown in Fig. 21(b), a specific V_{VAR} can produce a maximum output

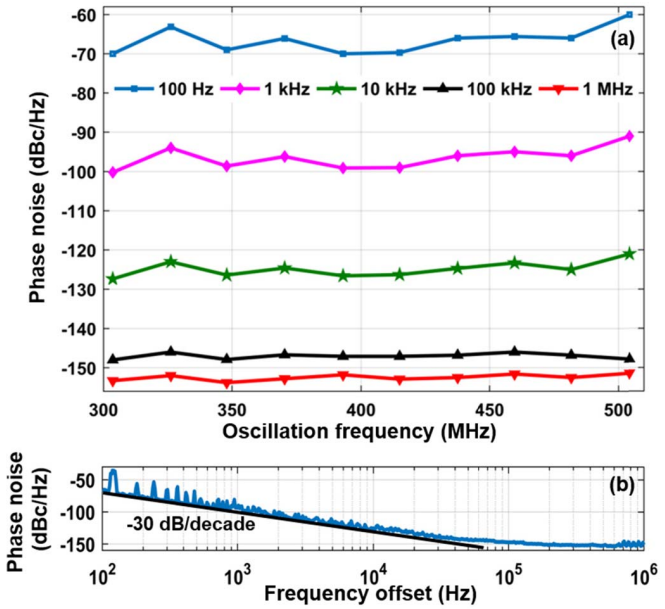

Fig. 22. (a) Phase noise of the ten locked modes at different frequency offsets. (b) Phase noise plot of the 415-MHz mode.

power of 0 dBm for each tone across their continuous tuning range. The VCMO consumes only 9 mW in operation due to the high FOM of the LOBAR.

Phase noise measurements were done with an Agilent E5052A Signal Source Analyzer and are reported in Fig. 22. The VCMO demonstrates on −100-dBc/Hz phase noise at 1-kHz offset from a 300-MHz carrier and the best noise floor of −153 dBc/Hz due to high FOMs of $LiNbO_3$ LOBARs. Fig. 22(b) shows the phase noise profile for the 415-MHz carrier as an example. The spurious profile is believed to be a result of the spurious resonance mode shown in Fig. 7(b).

An oscillator figure of merit FOM_{OSC} is defined below for a fair comparison of our work to the literature. FOM_{OSC} considers the oscillation frequency, the phase noise, and the power consumption metrics

$$\text{FoM}_{\text{OSC}} = -L(f_m) + 20\log\left(\frac{f_o}{f_m}\right) - 10\log\left(\frac{P_{\text{DC}}}{1\text{ mW}}\right) \quad (34)$$

where P_{dc} is the oscillator dc power consumption. Our VCMO is characterized with an FOM_{OSC} of 200 and 193 dBc/Hz at 1-kHz and 1-MHz offsets from a 300-MHz carrier.

V. Conclusion

Table II shows a performance summary and comparison to other reconfigurable MEMS oscillators. This article presents the highest number of locked tones of a single acoustic resonator with competitive phase noise and FOM_{OSC} results, making $LiNbO_3$ LOBAR VCMO a great candidate for direct RF synthesis deployed in wireless transceivers targeting multimode IoT applications. The tuning range and power consumption can be further enhanced via implementing the active circuitry in a recent-node CMOS. Moreover, having a switchable bank of tunable *LC* tanks with different inductor values would allow the VCMO to harness all the overtones provided by the LOBAR for a broader tuning range.

To have a fully continuous tuning range rather than a discrete one, the VCMO may lock to more closely packed resonances (i.e., a resonator with a smaller Δf). Hence, the LOBAR would have a larger width W_T, trading off k_t^2 of the resonances and inducing worse phase noise and larger power consumption in the oscillator. In addition, this solution requires a very high Q_{tank} and a widely reconfigurable filter to pick up the intended resonance. An alternative solution might be switching among a bank of LOBARs with a slightly different f_{center}. Only the LOBAR with the target resonance would be connected to the loop. This approach saves on power consumption and maintains the phase noise at the expense of a larger footprint. A third approach is to use an open fractional divider after the VCMO buffer to produce a continuous range of lower frequency carriers.

References

[1] R. Thirunarayanan, D. Ruffieux, and C. Enz, "Reducing energy dissipation in ULP systems: PLL-free FBAR-based fast startup transmitters," *IEEE Trans. Microw. Theory Techn.*, vol. 63, no. 4, pp. 1110–1117, Apr. 2015.

[2] P.-E. Su and S. Pamarti, "Fractional-N phase-locked-loop-based frequency synthesis: A tutorial," *IEEE Trans. Circuits Syst. II, Exp. Briefs*, vol. 56, no. 12, pp. 881–885, Dec. 2009.

[3] C.-M. Hsu, M. Z. Straayer, and M. H. Perrott, "A low-noise wide-BW 3.6-GHz digital $\Delta\Sigma$ fractional-N frequency synthesizer with a noise-shaping time-to-digital converter and quantization noise cancellation," *IEEE J. Solid-State Circuits*, vol. 43, no. 12, pp. 2776–2786, Dec. 2008.

[4] J. J. McCue *et al.*, "A time-interleaved multimode $\Delta\Sigma$ RF-DAC for direct digital-to-RF synthesis," *IEEE J. Solid-State Circuits*, vol. 51, no. 5, pp. 1109–1124, May 2016.

[5] A. Jerng and C. G. Sodini, "A wideband $\Delta\Sigma$ digital-RF modulator for high data rate transmitters," *IEEE J. Solid-State Circuits*, vol. 42, no. 8, pp. 1710–1722, Aug. 2007.

[6] A. Partridge, H.-C. Lee, P. Hagelin, and V. Menon, "We know that MEMS is replacing quartz. But why? And why now?" in *Proc. Joint Eur. Freq. Time Forum Int. Freq. Control Symp. (EFTF/IFC)*, Jul. 2013, pp. 1–6.

[7] C. Nguyen, "MEMS technology for timing and frequency control," *IEEE Trans. Ultrason., Ferroelectr., Freq. Control*, vol. 54, no. 2, pp. 251–270, Feb. 2007.

[8] A. Kourani, E. Hegazi, and Y. Ismail, "A 76.8 MHz temperature compensated MEMS reference oscillator for wireless handsets," *Microelectron. J.*, vol. 46, no. 6, pp. 496–505, Jun. 2015.

[9] R. Abdolvand, H. Lavasani, G. Ho, and F. Ayazi, "Thin-film piezoelectric-on-silicon resonators for high-frequency reference oscillator applications," *IEEE Trans. Ultrason., Ferroelectr., Freq. Control*, vol. 55, no. 12, pp. 2596–2606, Dec. 2008.

[10] K. E. Wojciechowski, R. H. Olsson, M. R. Tuck, E. Roherty-Osmun, and T. A. Hill, "Single-chip precision oscillators based on multi-frequency, high-Q aluminum nitride MEMS resonators," in *Proc. Int. Solid-State Sensors, Actuat. Microsyst. Conf.*, Jun. 2009, pp. 2126–2130.

[11] A. Kourani and S. Gong, "A tunable low-power oscillator based on high-Q lithium niobate MEMS resonators and 65-nm CMOS," *IEEE Trans. Microw. Theory Techn.*, vol. 66, no. 12, pp. 5708–5723, Dec. 2018.

[12] L. Colombo, A. Kochhar, C. Xu, G. Piazza, S. Mishin, and Y. Oshmyansky, "Investigation of 20% scandium-doped aluminum nitride films for MEMS laterally vibrating resonators," in *Proc. IEEE Int. Ultrason. Symp. (IUS)*, Sep. 2017, pp. 1–4.

[13] A. Ansari, "Single crystalline scandium aluminum nitride: An emerging material for 5G acoustic filters," in *IEEE MTT-S Int. Microw. Symp. Dig.*, May 2019, pp. 1–3.

[14] Z. Hao *et al.*, "Single crystalline ScAlN surface acoustic wave resonators with large figure of merit ($Q\times k_t^2$)," in *IEEE MTT-S Int. Microw. Symp. Dig.*, Jun. 2019, pp. 1–4.

[15] S. Gong and G. Piazza, "Design and analysis of Lithium–Niobate-based high electromechanical coupling RF-MEMS resonators for wideband filtering," *IEEE Trans. Microw. Theory Techn.*, vol. 61, no. 1, pp. 403–414, Jan. 2013.

[16] R. H. Olsson *et al.*, "A high electromechanical coupling coefficient SH0 Lamb wave lithium niobate micromechanical resonator and a method for fabrication," *Sens. Actuators A, Phys.*, vol. 209, pp. 183–190, Mar. 2014.

[17] R. H. Olsson *et al.*, "Lamb wave micromechanical resonators formed in thin film plates of Lithium Niobate," in *Proc. Int. Solid-State Sens., Actuat. Microsyst. Workshop*, Jun. 2014, pp. 281–284.

[18] R. Wang, S. A. Bhave, and K. Bhattacharjee, "Design and fabrication of s0 Lamb-wave thin-film lithium niobate micromechanical resonators," *J. Microelectromech. Syst.*, vol. 24, no. 2, pp. 300–308, Apr. 2015.

[19] R. Wang, S. A. Bhave, and K. Bhattacharjee, "High $k_t^2\times Q$, multifrequency lithium niobate resonators," in *Proc. IEEE 26th Int. Conf. Micro Electro Mech. Syst.*, Jan. 2013, pp. 165–168.

[20] G. W. Fang, G. Pillai, M.-H. Li, C.-Y. Liu, and S.-S. Li, "A VHF temperature compensated lithium niobate-on-oxide resonator with Q> 3900 for low phase noise oscillators," in *Proc. IEEE Micro Electro Mech. Syst. (MEMS)*, Jan. 2018, pp. 723–726.

[21] F. V. Pop, A. S. Kochhar, G. Vidal-Alvarez, and G. Piazza, "Laterally vibrating lithium niobate MEMS resonators with 30% electromechanical coupling coefficient," in *Proc. IEEE 30th Int. Conf. Micro Electro Mech. Syst. (MEMS)*, Jan. 2017, pp. 966–969.

[22] Y. Yang, R. Lu, T. Manzaneque, and S. Gong, "1.7 GHz Y-cut lithium Niobate MEMS resonators with FoM of 336 and fQ of 9.15×10^{12}," in *IEEE MTT-S Int. Microw. Symp. Dig.*, Jun. 2018, pp. 563–566.

[23] A. Kourani *et al.*, "A 150 MHz voltage controlled oscillator using lithium niobate RF-MEMS resonator," in *IEEE MTT-S Int. Microw. Symp. Dig.*, Jun. 2017, pp. 1307–1310.

[24] A. Kourani, R. Lu, T. Manzaneque, Y. Yang, A. Gao, and S. Gong, "A 175 MHz 72 μW voltage controlled oscillator with 1.4% tuning range based on lithium niobate MEMS resonator and 65 nm CMOS," in *IEEE MTT-S Int. Microw. Symp. Dig.*, Jun. 2018, pp. 567–570.

[25] M. Rinaldi, C. Zuo, J. Van der Spiegel, and G. Piazza, "Reconfigurable CMOS oscillator based on multifrequency AlN contour-mode MEMS resonators," *IEEE Trans. Electron Devices*, vol. 58, no. 5, pp. 1281–1286, May 2011.

[26] M. Rinaldi, C. Zuniga, B. Duick, and G. Piazza, "Use of a single multiplexed CMOS oscillator as direct frequency read-out for an array of eight AlN contour-mode NEMS resonant sensors," in *Proc. IEEE Sensors*, Nov. 2010, pp. 2666–2670.

[27] C. Zuo, N. Sinha, J. Van der Spiegel, and G. Piazza, "Multi-frequency pierce oscillators based on piezoelectric AlN contour-mode MEMS resonators," in *Proc. IEEE Int. Freq. Control Symp.*, May 2008, pp. 402–407.

[28] J. Stegner *et al.*, "A multi-frequency MEMS-based RF oscillator covering the range from 11.7 MHz to 1.9 GHz," in *IEEE MTT-S Int. Microw. Symp. Dig.*, Jun. 2018, pp. 575–578.

[29] C. Zuo, J. Van der Spiegel, and G. Piazza, "Dual-mode resonator and switchless reconfigurable oscillator based on piezoelectric AlN MEMS technology," *IEEE Trans. Electron Devices*, vol. 58, no. 10, pp. 3599–3603, Oct. 2011.

[30] H. M. Lavasani, R. Abdolvand, and F. Ayazi, "Single-resonator dual-frequency AIN-on-Si MEMS oscillators," *IEEE Trans. Ultrason., Ferroelectr., Freq. Control*, vol. 62, no. 5, pp. 802–813, May 2015.

[31] H. Zhang, W. Pang, H. Yu, and E. S. Kim, "High-tone bulk acoustic resonators on sapphire, crystal quartz, fused silica, and silicon substrates," *J. Appl. Phys.*, vol. 99, no. 12, Jun. 2006, Art. no. 124911.

[32] W. Pang, H. Zhang, J. J. Kim, H. Yu, and E. S. Kim, "High-tone bulk acoustic resonator integrated with surface micromachined FBAR filter on a single chip," in *IEEE MTT-S Int. Microw. Symp. Dig.*, Jun. 2005, pp. 2057–2060.
[33] H. Yu *et al.*, "HBAR-based 3.6 GHz oscillator with low power consumption and low phase noise," *IEEE Trans. Ultrason., Ferroelectr., Freq. Control*, vol. 56, no. 2, pp. 400–403, Feb. 2009.
[34] N. Chretien *et al.*, "Double-port AlN/Sapphire high overtone bulk acoustic resonators for the stabilization of radio-frequency oscillators," in *Proc. IEEE Int. Ultrason. Symp. (IUS)*, Oct. 2012, pp. 2210–2213.
[35] B. P. Sorokin *et al.*, "AlN/single crystalline diamond piezoelectric structure as a high overtone bulk acoustic resonator," *Appl. Phys. Lett.*, vol. 102, no. 11, Mar. 2013, Art. no. 113507.
[36] S. Gong, N.-K. Kuo, and G. Piazza, "GHz AlN lateral overmoded bulk acoustic wave resonators with af. Q of 1.17×10^{13}," in *Proc. Joint Conf. IEEE Int. Freq. Control Eur. Freq. Time Forum (FCS)*, May 2011, pp. 1–5.
[37] M. Ziaei-Moayyed, S. D. Habermehl, D. W. Branch, P. J. Clews, and R. H. Olsson, "Silicon carbide lateral overtone bulk acoustic resonator with ultrahigh quality factor," in *Proc. IEEE 24th Int. Conf. Micro Electro Mech. Syst. (MEMS)*, Jan. 2011, pp. 788–792.
[38] N.-K. Kuo *et al.*, "Micromachined sapphire GHz lateral overtone bulk acoustic resonators transduced by aluminum nitride," in *Proc. IEEE 25th Int. Conf. Micro Electro Mech. Syst. (MEMS)*, Jan. 2012, pp. 27–30.
[39] R. Lu, T. Manzaneque, Y. Yang, A. Kourani, and S. Gong, "Lithium niobate lateral overtone resonators for low power frequency-hopping applications," in *Proc. IEEE Micro Electro Mech. Syst. (MEMS)*, Jan. 2018, pp. 751–754.
[40] R. Lu, T. Manzaneque, Y. Yang, J. Zhou, H. Hassanieh, and S. Gong, "RF filters with periodic passbands for sparse Fourier transform-based spectrum sensing," *J. Microelectromech. Syst.*, vol. 27, no. 5, pp. 931–944, Oct. 2018.
[41] A. Kourani, R. Lu, A. Gao, and S. Gong, "A 300-500 MHz tunable oscillator exploiting ten overtones in single lithium niobate resonator," in *Proc. Joint Conf. IEEE Int. Freq. Control Symp. Eur. Freq. Time Forum (EFTF/IFC)*, Apr. 2019, pp. 1–4.
[42] I. E. Kuznetsova, B. D. Zaitsev, S. G. Joshi, and I. A. Borodina, "Investigation of acoustic waves in thin plates of lithium niobate and lithium tantalate," *IEEE Trans. Ultrason., Ferroelectr., Freq. Control*, vol. 48, no. 1, pp. 322–328, Jan. 2001.
[43] T. H. Lee and A. Hajimiri, "Oscillator phase noise: A tutorial," *IEEE J. Solid-State Circuits*, vol. 35, no. 3, pp. 326–336, Mar. 2000.
[44] U. L. Rhode, *Microwave and Wireless Synthesizers: Theory and Design*. Hoboken, NJ, USA: Wiley, 1997.
[45] D. B. Leeson, "A simple model of feedback oscillator noise spectrum," *Proc. IEEE*, vol. 54, no. 2, pp. 329–330, Feb. 1966.
[46] Y. Wang, Y. Hong, W. L. Goh, K. T. C. Chai, and M. Je, "A resonator-adaptable oscillator using varactor-loaded tuned amplifiers," *IEEE Microw. Wireless Compon. Lett.*, vol. 27, no. 8, pp. 724–726, Aug. 2017.

Ali Kourani (Graduate Student Member, IEEE) received the B.Sc. degree (Hons.) in electronics and communications engineering from Ain Shams University, Cairo, Egypt, in 2012, and the M.Sc. degree from The American University, Cairo, in 2015. He is currently pursuing the Ph.D. degree in electrical engineering with the University of Illinois at Urbana–Champaign (UIUC), Urbana, IL, USA.

From 2012 to 2016, he was an Analog/RF IC Researcher with the Zewail City of Science and Technology, Cairo, where he was involved in designing and developing sub-ppm frequency-stable RF MEMS reference oscillators for LTE. In 2015, he joined the CMOS Imaging Sensors Team, IMEC, Leuven, Belgium, as a Visiting Scholar, where he was responsible for the design and development of smart CMOS temperature sensors. In 2019, he joined the Mobile Business Unit, Skyworks Inc., Cedar Rapids, IA, USA, as an Engineering Intern, where he was involved in designing and developing the next-generation RF power amplifiers supporting 5G in cellular phones. His current research interests include microelectromechanical system-based wireless transceivers, and RF/mm-wave IC design.

Mr. Kourani received the MTT-S Graduate Fellowship in 2020, the Best Student Paper Award from the International Frequency Control Symposium, and the European Frequency and Time Forum (IFCS-EFTF) in 2019, the Paul D. Coleman Outstanding Research Award from the ECE Department, University of Illinois at Urbana–Champaign (UIUC), in 2019, the Commitment Recognition Award from Skyworks Inc., in 2019, the IEEE UFFC Student Travel Grant Award in 2019, the Dean Certificate of Honor from the School of Science and Engineering, American University in Cairo in 2014, the American University in Cairo Graduate Fellowship in 2013, and the Zewail City of Science and Technology Fellowships in 2012, 2013, and 2014. He serves as a reviewer for the IEEE TRANSACTIONS ON CIRCUITS AND SYSTEMS I.

Ruochen Lu (Member, IEEE) received the B.E. degree (Hons.) in microelectronics from Tsinghua University, Beijing, China, in 2014, and the M.S. and Ph.D. degrees in electrical engineering from the University of Illinois at Urbana–Champaign (UIUC), Urbana, IL, USA, in 2017 and 2019, respectively.

He is currently a Postdoctoral Researcher with UIUC. His research interests include radio frequency microsystems and their applications for timing and signal processing.

Dr. Lu received the Best Student Paper Awards at the 2017 IEEE International Frequency Control Symposium and 2018 IEEE International Ultrasonics Symposium, the 2015 Lam Graduate Award from the College of Engineering, UIUC, the 2017 Nick Holonyak, Jr. Graduate Research Award, the 2018 Nick Holonyak, Jr. Fellowship, and the 2019 Raj Mittra Outstanding Research Award from the Department of Electrical and Computer Engineering, UIUC.

Songbin Gong (Senior Member, IEEE) received the Ph.D. degree in electrical engineering from the University of Virginia, Charlottesville, VA, USA, in 2010.

He is currently an Associate Professor and the Intel Alumni Fellow with the Department of Electrical and Computer Engineering and the Micro and Nanotechnology Laboratory, University of Illinois at Urbana–Champaign, Urbana, IL, USA. His research primarily focuses on the design and implementation of radio frequency microsystems, components, and subsystems for reconfigurable RF front ends. In addition, his research explores hybrid microsystems based on the integration of MEMS devices with photonics or circuits for signal processing and sensing.

Dr. Gong was a recipient of the 2014 Defense Advanced Research Projects Agency Young Faculty Award, the 2017 NASA Early Career Faculty Award, the 2019 UIUC College of Engineer Dean's Award for Excellence in Research, the 2019 Ultrasonics Early Career Investigator Award, the Best Paper Awards from the 2017 and 2019 IEEE International Frequency Control Symposium and the 2018 and 2019 International Ultrasonics Symposium, and the 2nd place in Best Paper Competition at the 2018 IEEE International Microwave Symposium. He is a Technical Committee Member of the MTT-21 RF-MEMS of the IEEE Microwave Theory and Techniques Society, International Frequency Control Symposium, and International Electron Devices Meeting. He currently serves as the Chair for MTT TC6 and an Associate Editor for TUFFC and JMEMS.